Article | Open Access

Energy Materials

Chen *et al. Energy Mater.* **2026**, *6*, 600160 **DOI:**10.20517/energymater.2026.256

High-voltage flat-tubular segment-in-series SOFCs: strategic design of an $SrZrO_3$ insulation layer

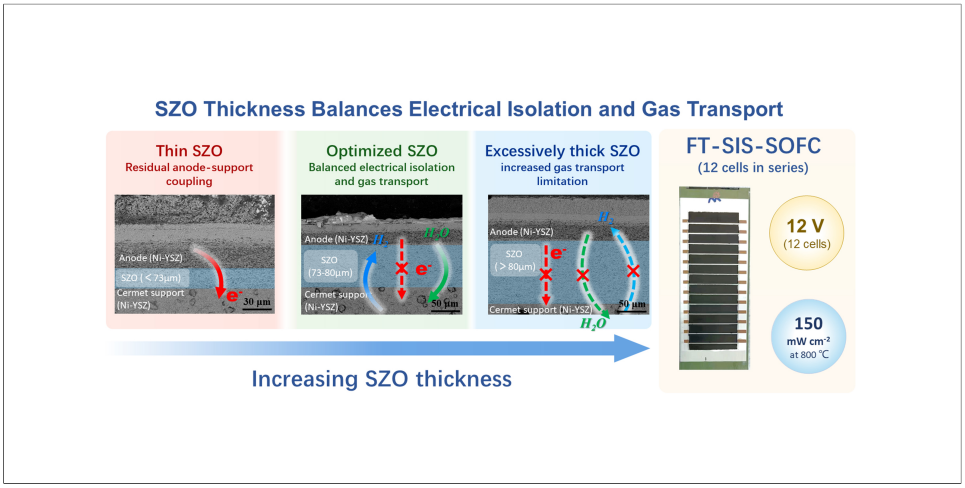
Ruyan Chen[1], Xiangxiang Pan[2], Haoyu Jiao[2], Tengfei Ma[1], Yanan Li[1], Shuwu Xu[3], Changqing Liu[1,*], Cheng-Xin Li[1,*]

Keywords:
Solid oxide fuel cells, segmented-in-series, flat-tubular, $SrZrO_3$, insulating layer

Citation: Chen, R.; Pan, X.; Jiao, H.; Ma, T.; Li, Y.; Xu, S.; Liu, C.; Li, C. X. High-voltage flat-tubular segment-in-series SOFCs: strategic design of an $SrZrO_3$ insulation layer. *Energy Mater.* **2026**, *6*, 600160. https://dx.doi.org/10.20517/energymater.2026.256

Received: 1 Aug 2026
First Decision: 11 Sep 2026
Revised: 29 Sep 2026
Accepted: 20 Oct 2026
Published: 19 Nov 2026

Academic Editor: Hong Li
Copy Editor: Ping Zhang
Production Editor: Ping Zhang



Abstract

Flat-tubular segment-in-series solid oxide fuel cells (FT-SIS-SOFCs) offer a promising route for high-voltage SOFC systems; however, current leakage through conductive cermet supports remains a critical challenge, and the design principles for porous insulating layers that simultaneously provide electrical decoupling and sufficient gas transport have not been fully established. Herein, porous insulating layers were introduced between the support and the anode of an FT-SIS-SOFC to suppress current leakage through the cermet support and preserve gas transport. $SrZrO_3$ (SZO) is a promising insulating material as it shows a stable perovskite structure at high temperatures and under a reducing atmosphere, and its resistivity is sufficiently high. Single cells with SZO insulating layer thicknesses from 0 μm to 108 μm were fabricated, and their performance exhibited a nonmonotonic thickness dependence. Thin SZO layers resulted in residual coupling between the anode and support, which introduced additional polarization. By contrast, excessively thick layers increased gas-transport resistance. The maximum anode-cathode (A-C) power density was achieved at an SZO thickness of approximately 73 μm, while a thickness range of 73-80 μm was identified as the practical optimal window for balancing

[1]State Key Laboratory for Mechanical Behavior of Materials, School of Materials Science and Engineering, Xi'an Jiaotong University, Xi'an 710049, Shaanxi, China.
[2]Shandong Moon Hydrogen Technology Research Institute Co., Ltd., Yantai 264006, Shandong, China.
[3]Moon Environment Technology Co., Ltd., Yantai 264002, Shandong, China.

***Correspondence to:** Dr. Changqing Liu, Prof. Cheng-Xin Li, State Key Laboratory for Mechanical Behavior of Materials, School of Materials Science and Engineering, Xi'an Jiaotong University, Xi'an 710049, Shaanxi, China. E-mail: liuchangqing@xjtu.edu.cn; licx@mail.xjtu.edu.cn

electrical decoupling and gas transport. Using this optimized design, a 14-cell FT-SIS-SOFC was fabricated, with 12 cells effectively connected in series for power generation. The device delivered an open-circuit voltage of 12 V at 700 °C and a peak power density of 150 mW cm^{-2} at 800 °C. These results demonstrate the feasibility of porous SZO as an insulating layer for high-voltage FT-SIS-SOFCs.

INTRODUCTION

Solid oxide fuel cells (SOFCs) are a promising technology for clean power generation. They directly convert chemical energy into electrical energy and produce low levels of harmful gas emissions[1], while also offering a high energy conversion efficiency and good fuel flexibility. These features make them suitable for distributed power generation and mobile power applications[2,3]. However, the output voltage of a single cell is usually limited to approximately 1.2 V. Therefore, practical systems commonly integrate multiple cells into stacks to achieve the required power output and operating voltage[4,5].

SOFC stacks are constructed using planar or tubular segment-in-series architectures[6]. Figure 1 compares the planar and flat-tubular (FT) configurations of these systems, wherein the planar stack achieves high power density because its paths for vertical conduction are short. However, assembly involves stacking external metallic interconnects and seals layer by layer. This process introduces challenges related to material compatibility and sealing stability over long periods[7].

In a flat-tubular segment-in-series SOFC (FT-SIS-SOFC), multiple single cells are integrated on a common support. These segments are electrically connected in series within a monolithic structure [Figure 2A], reducing reliance on external interconnects and intercell seals[6,8]. The resulting high-voltage and low-current output can also reduce resistive losses in conductors and power-conditioning components at a given power level[9,10].

Conventional FT-SIS-SOFCs use electrically insulating and chemically stable ceramic supports, including calcium-stabilized zirconia (CSZ) and $MgAl_2O_4$ [11,12]. Because these supports are electrically insulating, separate electrical terminals must be connected to the cathode and anode at opposite ends. This arrangement increases the difficulty of electrical connection and stack assembly. We previously developed a cermet-supported FT-SIS-SOFC in which the conductive metallic phase allows the two terminal leads to be collected from the same end[13]. This structure simplifies electrical connection and improves the practical assembly of the SOFC. The cermet support provides the mechanical framework required for fabricating and operating the cell with multiple layers. In addition, it serves as an electronically conductive pathway.

However, this system exhibits a drawback, as the high electronic conductivity of the cermet support introduces a bypass pathway with low resistance between the single cells and the common support. As illustrated in Supplementary Figure 1A and B, current can transfer from the anode to the conductive support instead of flowing through the intended series pathway. The resistance of the pathway through the support can be lower than the internal resistance of a cell, so the measured output voltage tends to approach that of a single cell. Consequently, the intended series connection is not achieved. An electrically resistive layer is needed between the conductive support and the anode to suppress current leakage [Supplementary Figure 1C and D]. This layer retains sufficient porosity for gas transport as it serves as the passageway for fuel to reach the anode.

An effective insulating layer for this architecture should maintain high electrical resistance under reducing conditions, remain compatible with other functional layers during co-sintering and operation, and exhibit suitable thermomechanical properties. $SrZrO_3$ (SZO) is a perovskite oxide whose crystal structure and

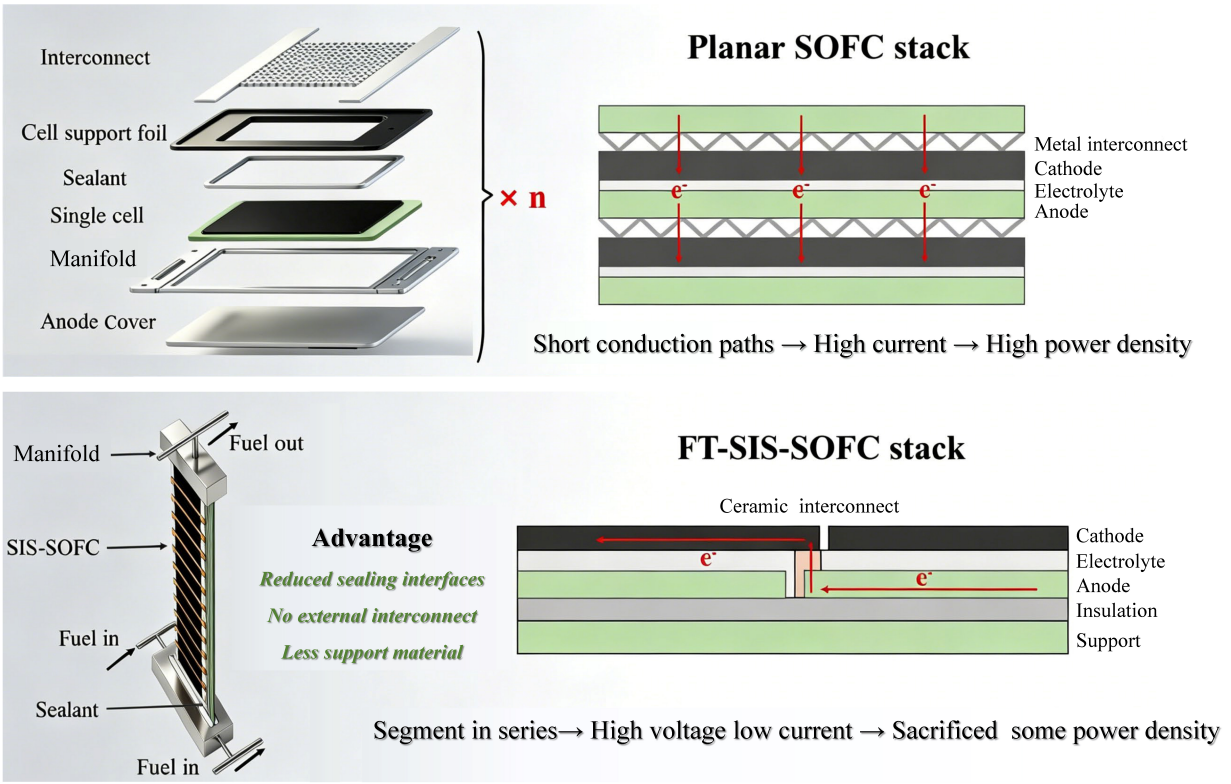


Figure 1. Schematic comparison between a planar SOFC stack and an FT-SIS-SOFC stack. FT-SIS-SOFC: Flat-tubular segment-in-series solid oxide fuel cell.

thermophysical properties have been investigated[14-17]. Previous studies have reported a thermal expansion coefficient (TEC) of approximately 9.7 - 10.9 × 10^{-6} K^{-1}[15,17]. This value is close to that of yttria-stabilized zirconia (YSZ), which may help reduce thermal expansion mismatch in the multilayer structure.

In conventional SOFC research, SZO is often considered an unwanted insulating phase that can form at the interface between the cathode and electrolyte through reactions[18-20]. The formation of this phase may increase interfacial resistance and affect long-term stability. In the present study, the electronic insulating property of SZO is used as a functional advantage. The high electrical resistivity of SZO under reducing conditions makes it a promising barrier for suppressing current leakage between the anode and the support. Therefore, a phase that is generally considered harmful in conventional SOFC interfaces is used as a functional insulating layer to enable high-voltage output from an FT-SIS-SOFC.

In this study, porous SZO insulating layers with different thicknesses were introduced between a cermet support and the anode in an FT-SIS-SOFC to suppress current leakage through the support while maintaining sufficient gas transport. The phase stability, sintering behavior, thermomechanical compatibility, and resistivity of SZO were evaluated. Single cells with varied SZO thicknesses were fabricated to investigate how the insulating layer affects the electrochemical behavior, which depends on the terminal configuration, the coupling between the anode and the support, and gas permeability. Based on the optimized thickness, a 14-cell FT-SIS-SOFC with 12 cells effectively connected for power generation was fabricated to demonstrate the practical utility of the porous SZO layer in a high-voltage monolithic stack.

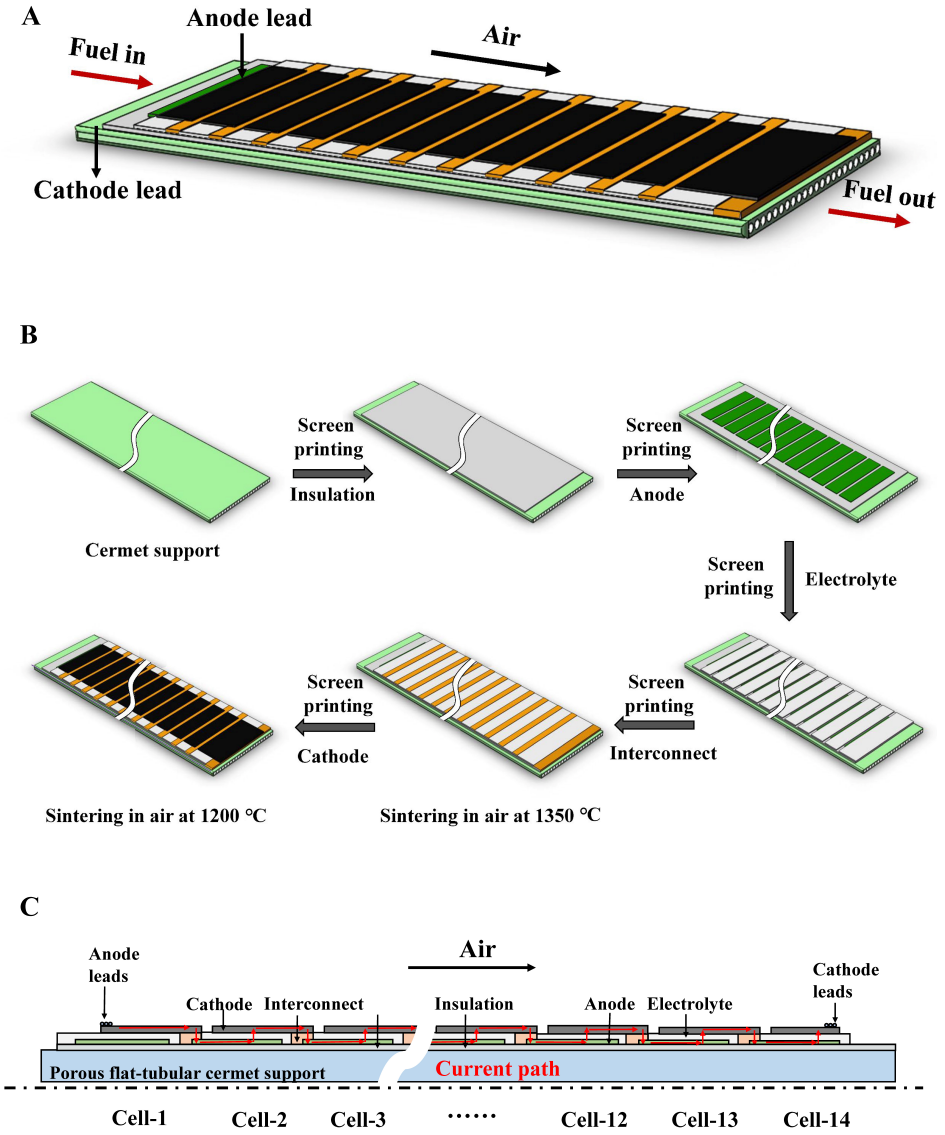


Figure 2. Schematic and fabrication process of the FT-SIS-SOFC. (A) Schematic of an FT-SIS-SOFC; (B) Flowchart of the FT-SIS-SOFC fabrication process; (C) Schematic of the current path through the 12 effective cells (Cell-2 to Cell-13) in the nominal 14-cell FT-SIS-SOFC. FT-SIS-SOFC: Flat-tubular segment-in-series solid oxide fuel cell.

EXPERIMENTAL

Preparation and characterization of SZO specimens

Commercial SZO powder (≥ 99%, metal basis; product No. S119235) was purchased from Shanghai Aladdin Biochemical Technology Co., Ltd. (Shanghai, China). The SZO powder was ground and mixed with a binder. The resulting mixture was uniaxially pressed at 200 MPa to form rectangular bars and circular pellets. The rectangular bars measured 35 × 8 × 3 mm^3, and the pellets had a diameter of 12.7 mm and a thickness of 3 mm. The green compacts were sintered in air at 1,350 °C for 4 h. To evaluate the phase compatibility of SZO with the adjacent cell materials, SZO-YSZ and SZO-NiO powder mixtures underwent heat treatment in air at 1,350 °C for 4 h, corresponding to the co-sintering condition used for cell fabrication, and they were subsequently characterized by X-ray diffraction (XRD, Empyrean, Malvern Panalytical, the Netherlands).

The morphology of the SZO powder and microstructure of the sintered specimens were examined by scanning electron microscopy (SEM, Hitachi S-3400, Hitachi High-Technologies Corporation, Japan). The phase compositions of the specimens sintered in air and reduced in H_2 were examined by XRD. The sintering

Table 1. Materials used for the functional layers of the cells

Functional layer	Material
Insulation	$SrZrO_3$ (Aladdin) with 10 wt.% graphite
Anode	NiO (Terio)-YSZ (Tosoh) with 5 wt.% graphite
Electrolyte	YSZ (Tosoh)
Interconnect	$La_{0.3}Sr_{0.7}TiO_3$ (Terio)
Cathode	$La_{0.8}Sr_{0.2}MnO_3$ (Terio)-YSZ (Tosoh)

YSZ: Yttria-stabilized zirconia.

shrinkage and TEC of the dense rectangular bars were measured using a thermal expansion analyzer (ZRPY-III-1600, Xiangtan Instrument and Apparatus Co., Ltd., China). The TEC of the sintered rectangular specimens was measured from 600 to 1,000 °C at a heating rate of 5 °C min^{-1} in air. The electrical resistivity of SZO was measured using a four-probe method (SI-1260, Solartron Analytical, UK) with Ag electrodes from 650 to 800 °C. Measurements were performed in air and H_2, with the latter reduced at 800 °C for 12 h prior to testing. To further evaluate the effect of water vapor, additional measurements were subsequently performed using the previously reduced SZO specimen. The specimen was first stabilized and measured under H_2 and then measured under humidified H_2 containing 3 vol.% H_2O using the same measurement procedure.

Fabrication and characterization of single cells

Single cells with different SZO layer thicknesses were fabricated on cermet-supported flat-tubular supports. The supports were supplied by the Shandong Industrial Ceramics Research & Design Institute and had dimensions of 60 × 74 mm. Screen printing inks for the functional layers were prepared by mixing the corresponding powders with ethyl cellulose and terpineol. Both organic materials were purchased from Shanghai Aladdin Biochemical Technology Co., Ltd. (Shanghai, China). The ratio of powder to organic medium was 4:6, and the materials used for the different functional layers are listed in Table 1. The mass ratio of NiO to YSZ in the anode was 6:4, and the mass ratio of $La_{0.8}Sr_{0.2}MnO_3$ to YSZ in the cathode was 5:5. The graphite contents were calculated relative to the total mass of the corresponding ceramic powders.

SZO insulating layers with different thicknesses were sequentially screen printed onto the cermet support. The anode and electrolyte layers, which had fixed thicknesses, were then printed onto the insulating layer. After drying, the support and printed insulating, anode, and electrolyte layers were co-sintered in air at 1,350 °C for 4 h. The cathode layer was subsequently screen printed onto the electrolyte and sintered in air at 1,200 °C for 2 h. A photograph of the fabricated cell is shown in Supplementary Figure 2A.

Gas permeability measurements

Additional specimens containing only the SZO insulating layer on the support were prepared for gas permeability measurements. During the test, compressed air first passed through a pressure regulator and a rotameter. It then passed through the specimen mounted in the test fixture. The pressure difference across the specimen was measured using a digital pressure gauge. The gas permeability was calculated using:

$$\mu = \frac{1.68875 \times 10^{10} \eta L q K_v}{A \Delta P} \quad (1)$$

where μ is the permeability of the specimen (mD), η is the dynamic viscosity of air at the test temperature (Pa s), L is the total thickness of the support and SZO (mm), A is the cross-sectional area for gas permeation (mm^2), ΔP is the pressure difference across the specimen (Pa), q is the reading of the rotameter ($mL \cdot min^{-1}$), and K_v is the water vapor correction factor, which is set to unity in this study. The unit conversion coefficient

was calculated based on the specified units and the standard conversion of 1 mD = 9.869233 × 10^{-16} m^2. The permeability measurements were conducted at room temperature. The effective permeation area was 25 cm^2 on each side. The two sides refer to the planar upper and lower surfaces of the specimen. Therefore, the total effective gas permeation area was 50 cm^2 (5,000 mm^2).

After permeability testing, representative support/SZO specimens were sectioned and examined by cross-sectional SEM. The porosities of the cermet support and SZO insulating layer were estimated from SEM images using ImageJ by applying a consistent thresholding procedure to distinguish the pore and solid phases.

Electrochemical characterization of single cells

The electrochemical performance of the single cells was measured using a four-probe method. Electrical terminals were connected to the support, cathode, and anode using silver paste. This arrangement allowed measurements under the support-cathode (S-C), anode-cathode (A-C), and support-anode (S-A) configurations. A photograph of the connected cell is shown in Supplementary Figure 2B. Before electrochemical testing, the cell was reduced in H_2 at 700 °C for 8 h. A photograph of the cell after reduction is shown in Supplementary Figure 2C. The effective active area of every single cell was 6 cm^2. The cell performance was then measured from 650 to 800 °C. H_2 was supplied to the anode at a flow rate of 0.3 L min^{-1}. Air was supplied to the cathode at 5 L min^{-1} using an air compressor. The voltage-current curves were recorded using a Keithley 2400 source meter (Keithley Instruments, USA). Electrochemical impedance spectroscopy (EIS) was performed using a Solartron SI-1260 electrochemical workstation. After electrochemical characterization, the cells were sectioned, and the thickness and microstructure of the SZO insulating layers were examined using cross-sectional SEM.

Fabrication and characterization of the FT-SIS-SOFCs

The FT-SIS-SOFCs were fabricated using screen printing. A cermet support supplied by the Shandong Industrial Ceramics Research & Design Institute was used. The support had dimensions of 185 × 74 mm, and the effective active area of each cell was 2 cm^2. Since the device contained 12 cells effectively connected in series for power generation, the total effective active area was 24 cm^2. The fabrication procedure was similar to that used for the single cells. The SZO insulating layer, anode, electrolyte, and interconnect layer were sequentially screen-printed and co-sintered in air at 1,350 °C for 4 h. The cathode layers were subsequently screen-printed and sintered in air at 1,200 °C for 2 h. The detailed fabrication process is illustrated in Figure 2B.

A nominal 14-cell FT-SIS-SOFC was fabricated. Cell-1 was used only as a terminal current collection region and did not participate in electrochemical power generation. During application of the diluted silver paste to the cathode surfaces, the cathode current collection regions of cell-13 and cell-14 became electrically connected. Consequently, cell-14 was bypassed and did not contribute to the output voltage. Therefore, the effective series-connected section consisted of 12 power-generating cells, comprising cell-2 to cell-13. This electrically active section is referred to hereafter as the 12-cell FT-SIS-SOFC. The current path and functions of the terminal regions are illustrated in Figure 2C. The output performance of the 12-cell FT-SIS-SOFC was measured using the four-probe method, and the voltage-current curves were recorded using a Keithley 2400 source meter. EIS measurements were performed using a Solartron SI-1260 electrochemical workstation. For these measurements, H_2 was supplied to the anode at a flow rate of 0.5 L min^{-1}, and air was supplied to the cathode at 8 L min^{-1} using an air compressor.

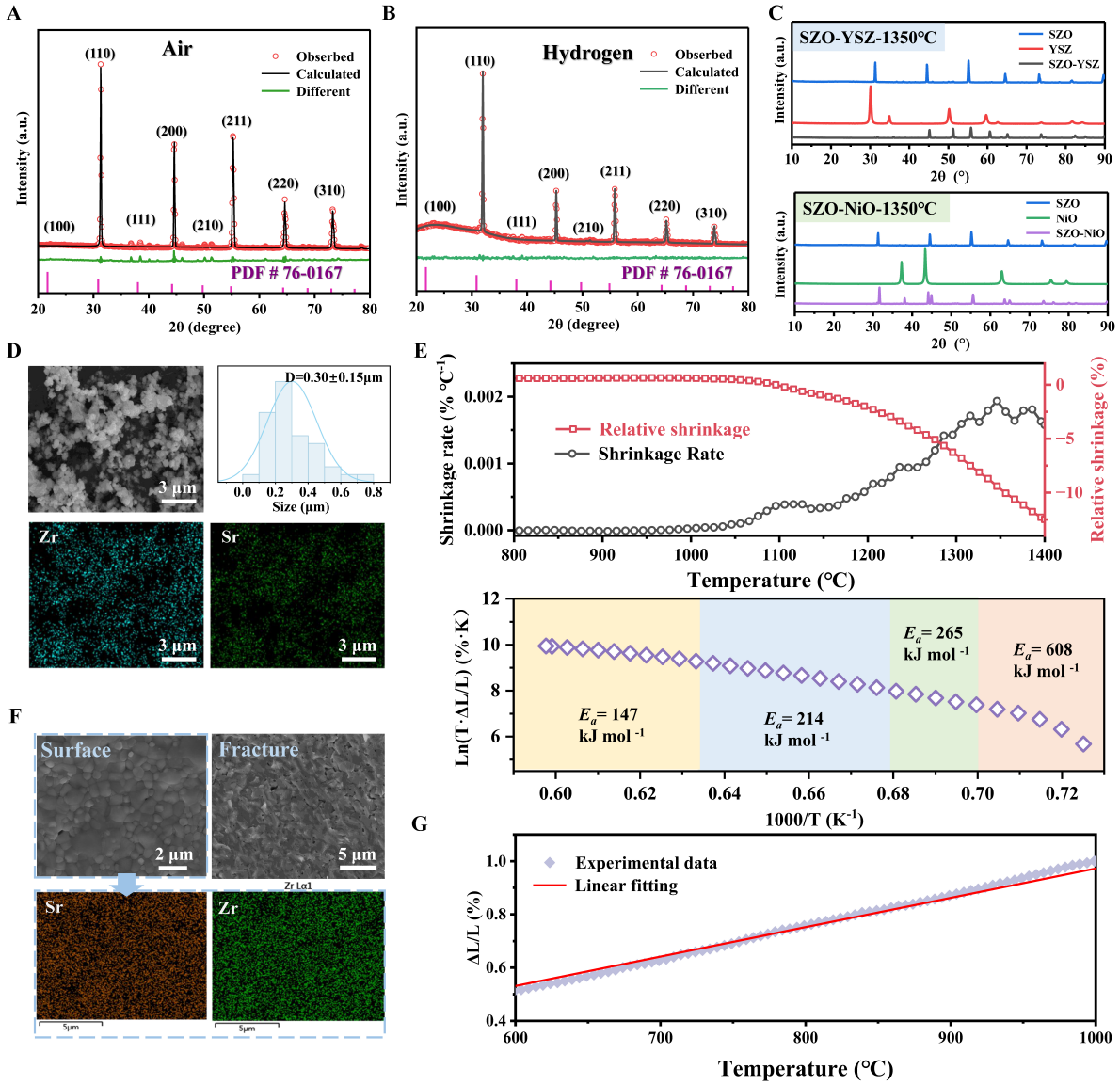


Figure 3. Phase composition, chemical compatibility, microstructure, sintering behavior, and thermomechanical properties of SZO. (A) XRD patterns of the sample sintered at 1,350 °C; (B) XRD patterns of the sample sintered at 1,350 °C and reduced at 800 °C for 12 h; (C) XRD patterns of SZO-YSZ and SZO-NiO powder mixtures after heat treatment at 1,350 °C for 4 h used to evaluate their phase compatibility; (D) SEM morphology, particle size distribution, and EDS elemental maps of SZO powder; (E) sintering behavior and apparent activation energy; (F) microstructure and elemental maps of the sintered specimen and (G) thermal expansion behavior. SZO: $SrZrO_3$; XRD: X-ray diffraction; YSZ: yttria-stabilized zirconia; SEM: scanning electron microscopy; EDS: energy-dispersive X-ray spectroscopy.

RESULTS AND DISCUSSION

Phase composition, sintering behavior, and thermomechanical properties of SZO

Figure 3A and B shows the XRD patterns of the SZO samples before and after reduction. The diffraction peaks of the sintered sample are in good agreement with the standard card for SZO (PDF#76-0167). The sample mainly shows a perovskite phase with no clearly detected secondary phase. After reduction, the main perovskite structure was retained. However, the main diffraction peaks shifted slightly toward higher angles, indicating a slight decrease in the corresponding lattice spacing. This change may be associated with defect formation during reduction, including oxygen loss and local lattice distortion[21,22].

The phase compatibility of SZO with YSZ and NiO was further evaluated using powder mixtures subjected to heat treatment at 1,350 °C, corresponding to the co-sintering temperature used for cell fabrication. As shown in Figure 3C, the diffraction patterns of the SZO-YSZ and SZO-NiO mixtures after heat treatment can be predominantly indexed to the corresponding constituent phases. No additional crystalline reaction products are clearly detected within the detection limit of the XRD analysis. These results indicate the good phase compatibility of SZO with YSZ and NiO under the applied co-sintering conditions.

The morphology and elemental distribution of the SZO powder are shown in Figure 3D. The powder consists of agglomerated submicron particles. The particle size distribution estimated from the SEM image is centered at approximately 0.3 μm. The energy-dispersive X-ray spectroscopy (EDS) elemental maps show that Sr and Zr are uniformly distributed. No additional elements were detected, consistent with the phase composition results obtained by XRD.

The sintering behavior of SZO is summarized in Figure 3E. Only limited shrinkage was observed below 1,000 °C. Clear shrinkage began above 1,000 °C, indicating the start of rapid densification. The densification rate remained low between 800 and 1,000 °C, then increased rapidly above 1,000 °C and reached its highest value between 1,300 and 1,350 °C. This behavior suggests that SZO changes from a slow densification stage to a rapid densification stage as the temperature increases. The relationship between shrinkage and the logarithm of the sintering temperature was used to estimate the apparent activation energy for SZO sintering. Four approximately linear regions were identified over different temperature ranges. The apparent activation energy decreased as the temperature increased. Below 1,150 °C, the steeper slope resulted in an activation energy of approximately 600 kJ mol^{-1}. However, the large error bars in this region indicate considerable uncertainty, which may be related to the low shrinkage rate during the early stage of sintering. At higher temperatures, the apparent activation energy decreased to 150 kJ mol^{-1}. This result suggests that densification becomes easier as the temperature increases, and the decrease may be related to enhanced atomic diffusion or structural rearrangement during sintering.

The microstructure of the SZO bulk sample sintered at 1,350 °C is shown in Figure 3F. The specimen exhibits a relatively compact and uniform microstructure, with an average grain size of approximately 1 μm. No obvious macroscopic cracks or large defects are observed, although a small number of residual pores remain visible. The corresponding EDS maps show uniform distributions of Sr and Zr. These observations indicate that the SZO powder can form a mechanically continuous ceramic structure under the selected sintering conditions.

The linear thermal expansion (ΔL/L) curve of SZO from 600 to 1,000 °C is shown in Figure 3G. The relative length change increases monotonically with temperature, and the calculated average TEC is 11.6×10^{-6} K^{-1}. This value is close to those of the main functional layers in the SOFC, which may reduce thermal expansion mismatch during co-sintering and operation and lower the risk of cracking or delamination during thermal cycling.

Electrical transport behavior of SZO under oxidizing and reducing atmospheres

Figure 4 compares the electrical resistivity of the sintered SZO specimens measured in air and H_2. Figure 4A shows that the resistivity decreased continuously with increasing temperature, which is consistent with thermally activated conduction in semiconductor-like materials. At 650, 700, 750, and 800 °C, the resistivity values in H_2 were 1.74×10^5, 6.20×10^4, 1.81×10^4, and 7.40×10^3 Ω cm, respectively, whereas the corresponding values in air were 3.81×10^5, 1.69×10^5, 7.89×10^4, and 3.86×10^4 Ω cm. Therefore, the resistivity measured in H_2 was lower than that measured in air. This result suggests that the reducing atmosphere increases the concentration or mobility of charge carriers. This change may be related to

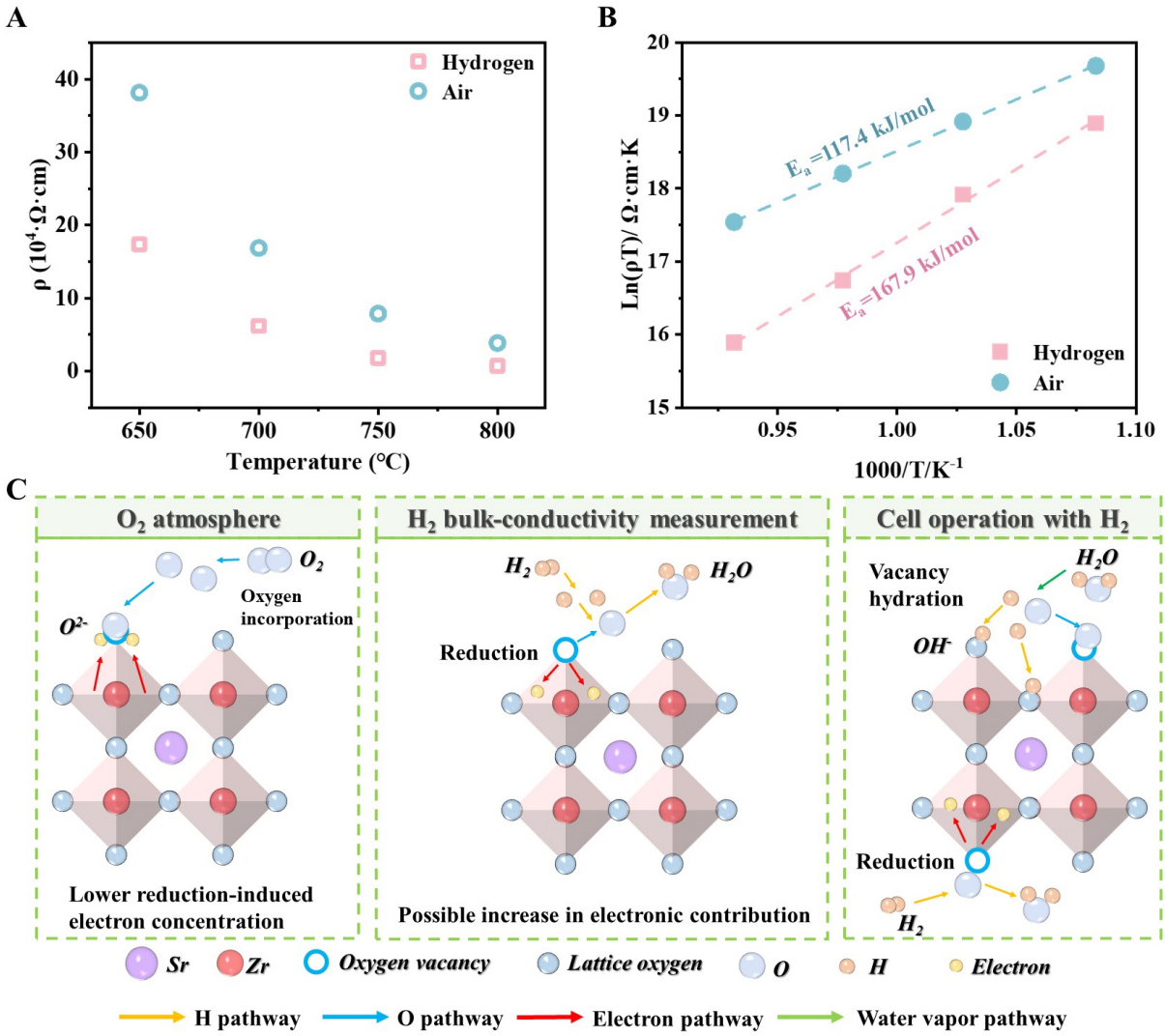


Figure 4. Electrical characterization of SZO. (A) Electrical resistivity of SZO measured in air and H_2 at different temperatures; (B) Arrhenius plots for SZO measured in air and H_2; and (C) schematic of the possible defect reactions occurring under oxidizing conditions, in H_2, and during cell operation with locally generated H_2O. SZO: $SrZrO_3$.

atmosphere-dependent defect reactions and conduction mechanisms[21,23]. In both atmospheres, the resistivity of SZO was approximately four orders of magnitude higher than that of the other SOFC functional layers. This high resistivity supports its use as an insulating material between the anode and the support.

Figure 4B shows the Arrhenius plots of $ln(\rho T)$ versus $1000/T$ for SZO measured in air and H_2. An approximately linear relationship was obtained in both atmospheres, indicating that the resistivity follows a thermally activated process. The apparent activation energies (E_a) calculated from the Arrhenius plots were 117.4 kJ mol^{-1} in air and 167.9 kJ mol^{-1} under H_2. The higher apparent activation energy in H_2 indicates a stronger temperature dependence of resistivity under the reducing atmosphere. Nevertheless, the resistivity measured in H_2 remained lower than that measured in air over the investigated temperature range, indicating that the absolute resistivity is also influenced by the charge carrier concentration and the pre-exponential factor.

A possible atmosphere-dependent interpretation based on defect chemistry is illustrated in Figure 4C. $SrZrO_3$-based materials may exhibit an increased n-type electronic contribution at low oxygen partial pressure, depending on their composition and defect chemistry[24]. Under oxidizing conditions, oxygen

incorporation consumes oxygen vacancies and electrons, whereas under a reducing atmosphere, oxygen removal may produce oxygen vacancies and electrons. The slight shift of the XRD peaks after reduction indicates a change in the average lattice spacing, which may be related to defect formation during reduction or residual lattice strain[22].

To further evaluate the electrical insulating behavior of SZO under conditions closer to cell operation, additional paired resistivity measurements were performed on the previously reduced SZO specimen under dry H_2 and humidified H_2 containing 3 vol.% H_2O [Supplementary Figure 3]. The resistivity under humidified H_2 was consistently slightly higher than that measured under dry H_2 over 650-800 °C, with an increase of approximately 2%-7%. Therefore, the introduction of 3 vol.% H_2O did not decrease the electrical resistivity of SZO under the investigated conditions, indicating that its insulating behavior was maintained under humidified reducing conditions. Under such humidified reducing conditions, reduction and hydration equilibria may coexist. Water vapor may hydrate available oxygen vacancies via[25]:

$$H_2O + V_O^{\cdot\cdot} + O_O^{\times} \rightleftharpoons 2OH_O^{\cdot} \tag{2}$$

These processes may decrease the electronic contribution from reduction while introducing protonic defects[22,25-27].

Microstructure and gas permeability of the support/SZO composite

Figure 5 shows cross-sectional SEM images of the active cell region with different SZO thicknesses. All cells exhibit the designed multilayer structure consisting of the cathode, dense electrolyte, anode, porous SZO insulating layer, and cermet support. The designed multilayer structure is maintained over the investigated thickness range, and the SZO layer remains continuous between the anode and cermet support without obvious macroscopic cracking or delamination. To quantitatively characterize the porous structure relevant to gas transport, ImageJ porosity analysis was performed. As shown in Supplementary Figure 4, the cermet support exhibits a porosity of approximately 30%, whereas the SZO insulating layer exhibits a somewhat lower porosity of approximately 23%-28%.

Cross-sectional SEM images of the support/SZO specimens used for the gas permeability measurements are further shown in Supplementary Figure 5. The SZO thickness ranges from 18 to 127 μm, and the porous SZO layers remain continuous throughout this range without obvious macroscopic structural failure. The corresponding apparent permeability results are shown in Supplementary Figure 6. The gas permeability remains relatively high at SZO thicknesses below approximately 80 μm, ranging from 0.66 to 0.73 mD. It subsequently decreases to approximately 0.56 mD at 99 μm and 0.38 mD at 108 μm, followed by a further decrease to approximately 0.04 mD at 127 μm. These results indicate that, although the SZO microstructure remains porous and structurally continuous, increasing the thickness of the somewhat lower-porosity SZO layer increases the gas transport distance and progressively increases its contribution to the overall transport resistance.

Performance of single cells dependent on the terminal configuration

Single cells with different SZO thicknesses were tested from 650 to 800 °C under fixed fuel and air flow rates. Figure 6A shows the A-C configuration, in which the external circuit is connected to the anode and cathode. This configuration represents the normal operating condition of the cell. Figure 6B shows the S-C configuration, in which the conductive support is used as the external terminal on the anode side. In this configuration, the oxygen ion transport path extends from the cathode through the electrolyte to the anode. The electrons produced at the anode then pass through the SZO layer before reaching the support (A-SZO-S). This configuration can therefore be used to evaluate the ability of the support to collect current through

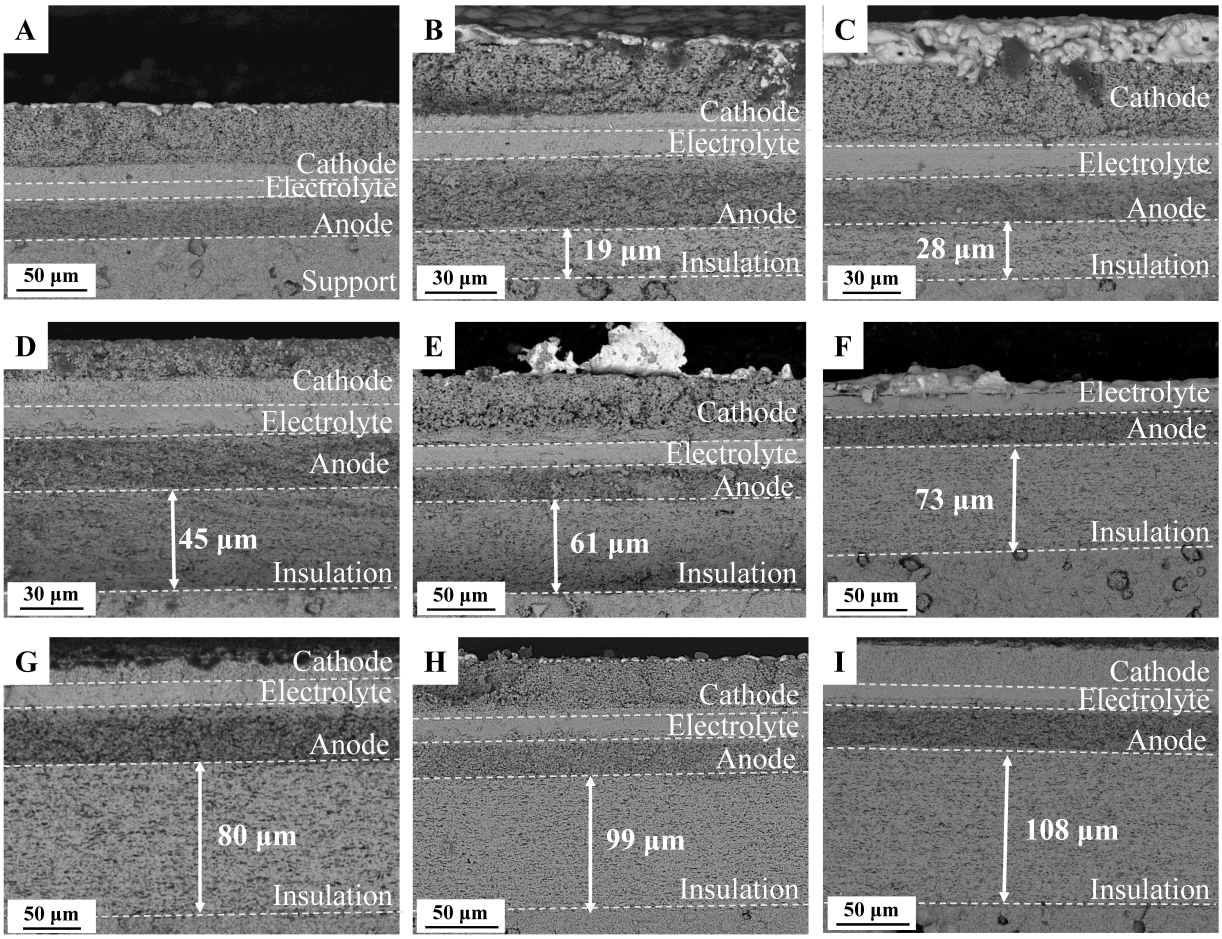


Figure 5. Cross-sectional SEM images of single cells with different SZO insulating layer thicknesses: (A) 0 μm, (B) 19 μm, (C) 28 μm, (D) 45 μm, (E) 61 μm, (F) 73 μm, (G) 80 μm, (H) 99 μm, and (I) 108 μm. SZO: $SrZrO_3$; SEM: scanning electron microscopy.

the SZO layer. Figure 6C shows the S-A configuration. This configuration is used as a diagnostic measurement of the electrical coupling between the anode and support.

The A-C configuration exhibited typical fuel cell polarization behavior, with open-circuit voltages (OCVs) of approximately 1 V [Supplementary Figure 7]. Figure 6D summarizes the power densities of cells with different SZO thicknesses. At 800 °C, the cell without an SZO layer reaches a peak power density of approximately 183 mW cm^{-2}. After the SZO layer is introduced, the power density first decreases. It reaches a minimum of approximately 76 mW cm^{-2} at an SZO thickness of around 28 μm. The power density then recovers and reaches its highest value of approximately 187 mW cm^{-2} at an SZO thickness of 73 μm, indicating that this thickness corresponds to the highest A-C power density among the tested cells at 800 °C. When the SZO thickness exceeds 80 μm, the power density decreases again, and this trend is not monotonic over the full temperature range of 650 to 800 °C.

In the A-C configuration, the external current is collected directly from the anode. Therefore, the SZO layer is not connected in series with the main electron output path. Cross-sectional SEM images also show no clear delamination or physical separation between the layers. Thus, the nonmonotonic A-C performance cannot be explained by the thickness-dependent resistance of the insulating layer. Instead, the results suggest that the loss mechanisms on the anode side change with SZO thickness. These mechanisms may include electrical coupling between the anode and support through the SZO layer[9,28]. They may also include gas transport

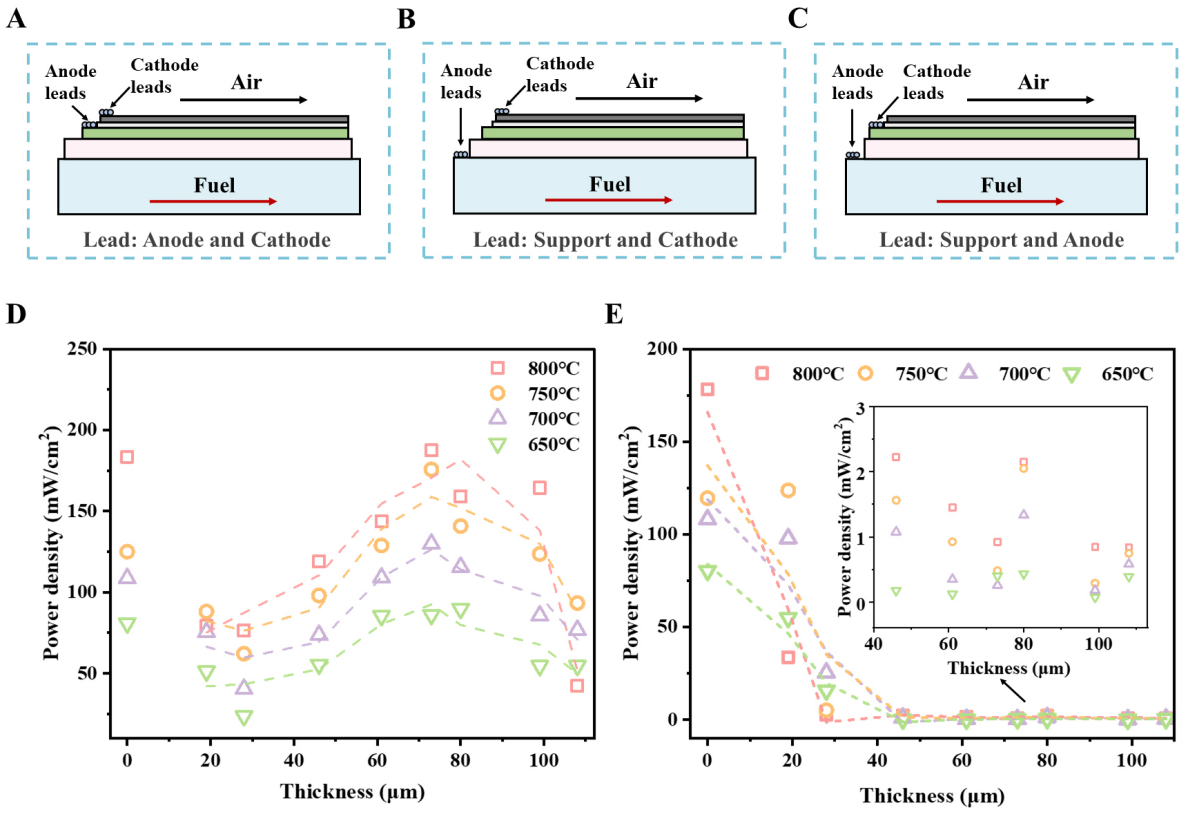


Figure 6. Effect of the SZO insulating layer thickness on the electrochemical performance of single cells with different terminal configurations. Schematics of the (A) A-C, (B) S-C, and (C) S-A configurations. Peak power density as a function of SZO thickness under the (D) A-C and (E) S-C configurations. The power densities were calculated based on an active area of 6 cm^2 for every single cell. SZO: $SrZrO_3$; A-C: anode-cathode; S-C: support-cathode; S-A: support-anode.

resistance when the SZO layer becomes too thick. Accordingly, gas transport limitation is considered a main reason for the second decrease in A-C output performance when the SZO thickness exceeds 80 μm.

The S-C configuration provides a more direct evaluation of the ability of the A-SZO-S pathway to carry current. As shown in Figure 6E, the S-C power density at 800 °C rapidly decreases from approximately 178 mW cm^{-2} without SZO to below 30 mW cm^{-2} at an SZO thickness of around 28 μm. It further decreases to approximately 2 mW cm^{-2} at around 45 μm. Beyond this thickness, the S-C output remains very low. This result demonstrates that increasing the SZO thickness suppresses the ability of the conductive support to collect operating current from the anode.

Although the S-C power output was low for thicker SZO layers, the corresponding OCV remained close to 1 V, as shown in Supplementary Figure 8. The persistence of a high OCV indicates that an electrochemical potential can still be established at the support terminal under negligible current conditions. However, sustained power generation requires a sufficiently conductive direct-current pathway between the anode and support. Therefore, the OCV alone does not demonstrate that the A-SZO-S pathway has a low resistance or a high current-carrying capacity. The rapid decrease in the S-C power output provides more direct evidence that this pathway becomes blocked as the SZO layer thickens.

The S-C current collection through the support becomes ineffective at approximately 45 μm. However, the best A-C performance was obtained at approximately 73 μm. This difference indicates that loss of current collection occurs before the A-C performance reaches its optimum. The support may retain a residual electrical coupling with the anode after it has lost the ability to carry the full operating current[9,28].

DC coupling and impedance analysis of the A-SZO-S pathway

The S-A polarization measurements were used to evaluate the residual electrical coupling between the anode and support. The closed circuit starts at the anode, passes through the SZO layer and its two interfaces, and reaches the support. The current then passes through the external testing system before returning to the anode. As shown in Supplementary Figure 9, the S-A voltage-current curves were approximately linear and can be expressed as

$$U_{S-A} = E_{S-A} - I_{S-A}R_{S-A} \tag{3}$$

where $E_{S\text{-}A}$ is the potential difference between the support and functional anode at zero applied current, and the slope-derived $R_{S\text{-}A}$ is defined here as an effective direct current resistance of the entire anode-SZO-support pathway. Moreover, the measured response may contain contributions from charge transport through the SZO layer, the anode/SZO and SZO/support interfaces, electrical contacts, local parallel conduction pathways, and other contributions that are approximately linear within the investigated DC current range. Because EIS was not measured directly under the S-A terminal configuration, these individual contributions to $R_{S\text{-}A}$ cannot be deconvoluted in the present study. Therefore, $R_{S\text{-}A}$ is used only to compare the relative strength of anode-support DC coupling among cells with different SZO thicknesses.

The $R_{S\text{-}A}$ values exhibit an overall tendency to increase with SZO thickness, although noticeable nonmonotonic variations are observed [Supplementary Table 1]. Specifically, $R_{S\text{-}A}$ increases from 14.5 Ω at 28 μm to 33.4 Ω at 73 μm, followed by a marked decrease to 14.8 Ω at 80 μm. It subsequently increases to 42.5 Ω at 99 μm before slightly decreasing to 38.0 Ω at 108 μm. These results suggest that, although thicker SZO layers generally tend to exhibit higher effective DC resistance, the relationship between $R_{S\text{-}A}$ and SZO thickness is not strictly monotonic. The observed variations may be associated with differences in interfacial contact, microstructural heterogeneity, and possible residual conductive pathways.

To obtain independent frequency-resolved information on the losses associated with the A-SZO-S pathway, EIS spectra measured under the A-C and S-C configurations were further analyzed using the distribution of relaxation times (DRT). Figure 7A shows the A-C impedance spectra at 800 °C. In this configuration, the measured impedance mainly includes the ohmic loss of the electrolyte, electrode reaction losses, gas diffusion and mass transfer polarization, and indirect effects from the support and insulating layer[29]. The overall impedance exhibits a nonmonotonic dependence on the SZO thickness, which is consistent with the corresponding A-C power density behavior. By contrast, the S-C impedance markedly increases when the SZO thickness reaches approximately 45 μm and above [Figure 7B], and the Nyquist response becomes strongly depressed and nonideal. The substantially larger S-C impedance indicates additional losses associated with current collection through the A-SZO-S pathway.

To resolve the overlapping impedance contributions, DRT analysis was applied to both configurations [Figure 7C and D]. The A-C spectra exhibit several distributed relaxation features over a broad frequency range, consistent with the overlapping polarization processes commonly observed in solid oxide cells[30]. By contrast, a pronounced high-frequency contribution develops in the thicker SZO S-C spectra, together with weaker contributions at intermediate and low frequencies. The DRT results therefore confirm that the depressed S-C Nyquist response contains multiple overlapping relaxation processes rather than a single polarization process.

Comparison of the A-C and S-C DRT spectra at representative SZO thicknesses [Supplementary Figure 10] shows that the pronounced high-frequency contribution is strongly enhanced specifically under the S-C configuration. Because the S-C current collection requires electrons to pass through the A-SZO-S pathway,

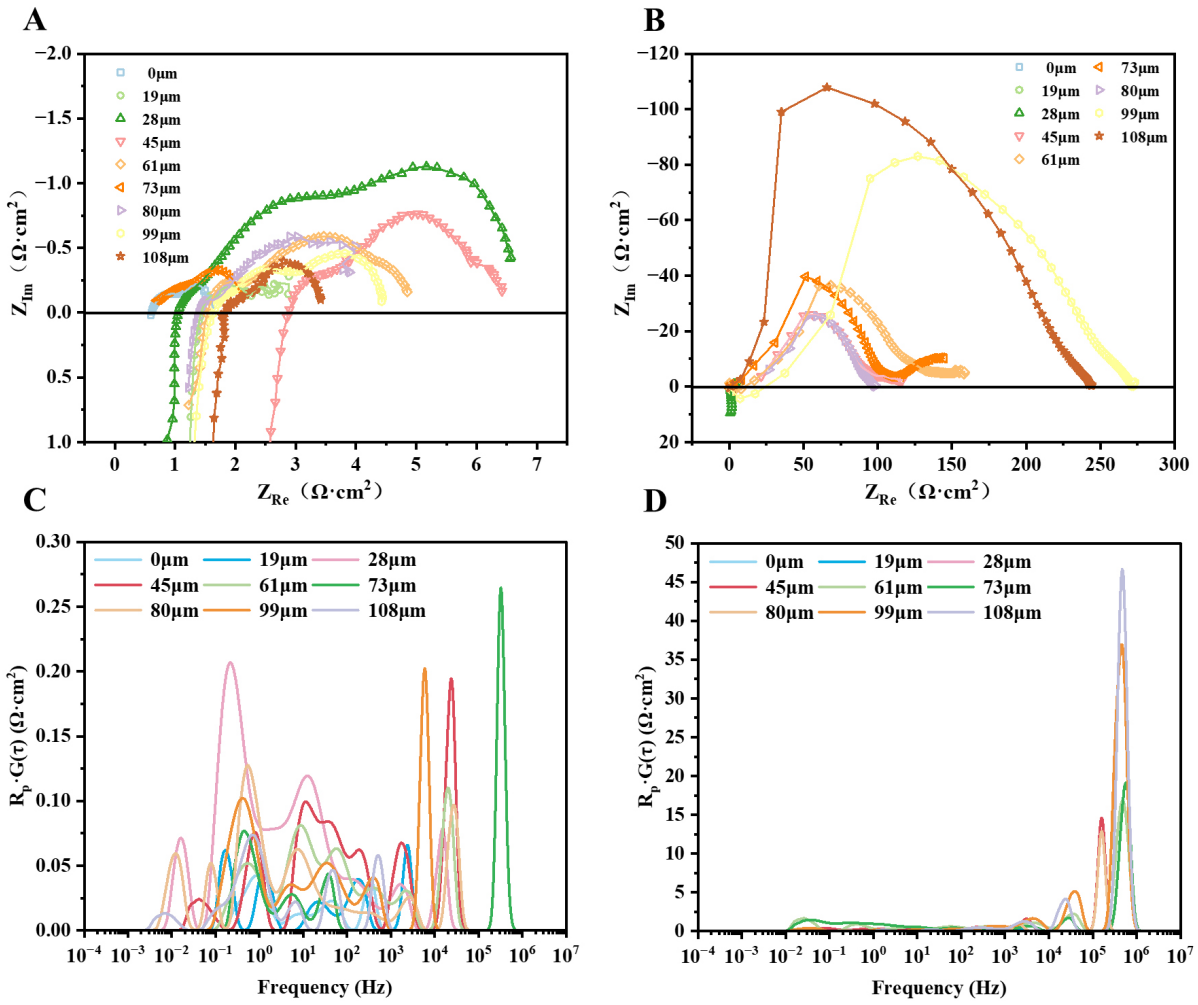


Figure 7. Impedance and distribution of relaxation times (DRT) analyses of single cells with different SZO insulating-layer thicknesses at 800 °C. (A) Nyquist spectra measured under the A-C configuration; (B) Nyquist spectra measured under the S-C configuration; (C) corresponding DRT spectra obtained under the A-C configuration; and (D) corresponding DRT spectra obtained under the S-C configuration. SZO: $SrZrO_3$; A-C: anode-cathode; S-C: support-cathode.

this contribution is associated with a fast electrical/interfacial response of this pathway. However, because EIS was not independently measured under the S-A configuration, the individual contributions of the SZO bulk, anode/SZO interface, and SZO/support interface cannot be uniquely separated. Therefore, these results support that the A-SZO-S pathway involves distributed electrical/interfacial processes.

Having established from the DRT analysis that the impedance spectra contain multiple overlapping relaxation contributions, the overall thickness dependence of the impedance magnitude was further compared using the apparent high-frequency, polarization, and total resistance values, as summarized in Supplementary Figure 11. These quantities are used here only to describe the overall evolution of the impedance magnitude.

In the A-C configuration [Supplementary Figure 11A], the total resistance exhibits a nonmonotonic dependence on the SZO thickness. At 800 °C, it increases from approximately 2 Ω cm² for the cell without SZO to approximately 7 Ω cm² at 28 μm, decreases again to approximately 2 Ω cm² at 73 μm, and then increases at greater thicknesses. This evolution is consistent with the initial decrease, subsequent recovery, and final decrease in the A-C peak power density. The high-frequency intercept resistance shows a smaller

variation than the apparent polarization contribution, indicating that the pronounced nonmonotonic change in the overall impedance is mainly reflected in the latter system. In the thin SZO region, the increased apparent polarization correlates with incomplete anode-support electrical decoupling, whereas the resistance increase at larger SZO thicknesses is consistent with the independently observed decrease in gas permeability.

A much larger impedance increase is observed under the S-C configuration [Supplementary Figure 11B]. The total resistance remains relatively low at SZO thicknesses of 19 and 28 μm but increases sharply to approximately 116 Ω cm² at 45 μm and remains large in the region with a thicker SZO layer, reaching 272 Ω cm² at 99 μm. The apparent polarization contribution similarly increases from 5.41 Ω cm² at 28 μm to 99.92 Ω cm² at 46 μm and reaches 248 Ω cm² at 99 μm, although substantial variation is observed among the specimens with a thicker SZO layer. The S-C impedance is therefore generally one to two orders of magnitude larger than the corresponding A-C impedance in the region with a thicker SZO layer, consistent with the rapid decrease in S-C power density shown in Figure 6E. As demonstrated by the DRT analysis in Figure 7, this large apparent resistance contains multiple distributed contributions associated with current collection through the A-SZO-S pathway rather than a single polarization process.

The potential relationships among the anode, support, and cathode were also examined at 800 °C. When measured at the same time and under the same conditions, these voltages should ideally satisfy

$$V_{S-A} = V_{S-C} - V_{A-C} \tag{4}$$

Supplementary Table 2 summarizes the open-circuit potentials and the closure deviations for cells with different SZO thicknesses. The measured $V_{S\text{-}A}$ values range from 0.031 to 0.129 V. The calculated $V_{S\text{-}A}$ using the common cathode reference range from 0.011 to 0.160 V. The two sets of values generally have the same sign and similar magnitudes, with an average absolute closure deviation of approximately 27 mV. Because the three voltages were sequentially measured, the deviations may include open-circuit drift and different stabilization states after terminal switching.

The nonzero $V_{S\text{-}A}$ values indicate that the support and anode behave as different electrical nodes after the introduction of the SZO layer. In the A-C configuration, the support acts as a floating conductive node whose potential is influenced by the finite S-A coupling and interfacial conditions. Combined with the S-A polarization and S-C impedance results, these measurements justify the equivalent circuit representation in which the support is modeled as a separate node that is not shorted to the anode.

Mechanism of thickness-dependent A-S electrical coupling

In SIS-SOFCs, a support with nonzero conductivity can provide an unintended shunting pathway between electrode regions. This pathway is driven by local potential differences that arise along the support. Previous modeling studies have shown that shunting currents are influenced by the electrical properties of the support and the local potential distribution, potentially leading to voltage and power losses[9,28]. In the present structure, the highly conductive cermet support is separated from the anode by the porous SZO layer. The SZO layer does not simply change the anode and support from a connected state to a completely disconnected state as its thickness increases. Instead, it gradually changes the electrical coupling between support and anode.

As illustrated in Figure 8A, the operating current in the A-C configuration is directly collected from the anode. In this configuration, the SZO layer is not connected in series with the principal external current path, and the support behaves as a floating node. Nevertheless, residual A-S coupling may still provide an internal

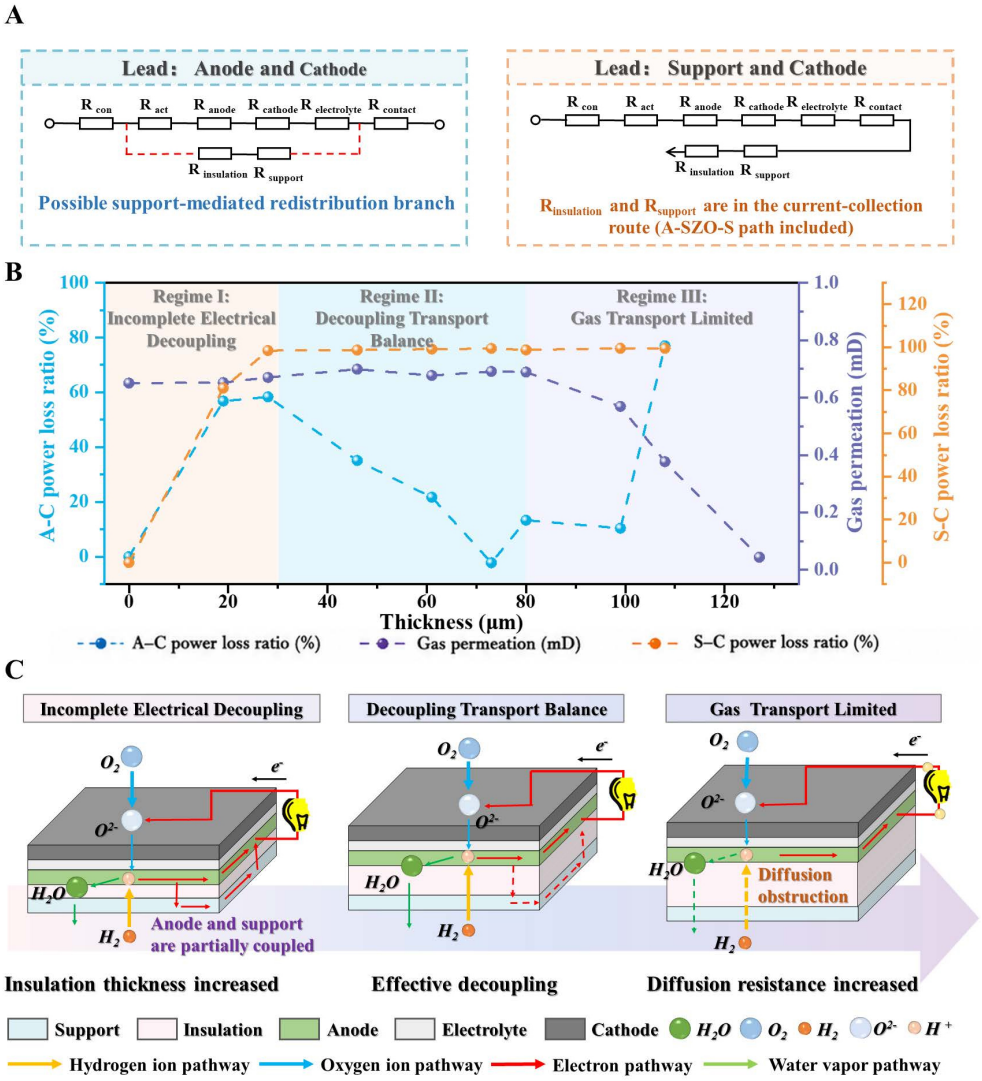


Figure 8. Effect of insulating-layer thickness on current coupling, power loss, and gas-transport behavior. (A) Simplified equivalent circuits for the A-C and S-C configurations; (B) evolution of the A-C power loss ratio, S-C power loss ratio, and gas permeability with the insulating layer thickness; and (C) schematic of the electron, oxygen ion, hydrogen, and water vapor transport pathways within the three thickness regimes. SZO: $SrZrO_3$; A-C: anode-cathode; S-C: support-cathode.

pathway for local current redistribution through the support. In the S-C configuration, the support serves as the external terminal on the anode side. Consequently, electrons generated at the anode must pass through the A-SZO-S pathway, which is now in series with the path for collecting electrons from the anode side.

The A-C and S-C power loss ratios were calculated as the reduction in peak power density relative to the corresponding reference cell without SZO. The combined results can be roughly divided into three regimes, as shown in Figure 8B and C. The boundaries between the three regimes are approximate because the tested thicknesses are discrete.

Without an SZO layer, the anode and the support are in direct contact and can be approximated as a common conductive node. The support can collect operating current efficiently, resulting in comparable and relatively high output under both the A-C and S-C configurations. At approximately 30 μm, electrical decoupling remains incomplete. The resulting A-C performance loss is attributed to residual S-A coupling. A plausible explanation is that local potential gradients along the anode drive current redistribution through

the support, which is consistent with the shunting behavior reported for conventional SIS-SOFCs.

When the SZO thickness increases to approximately 30-80 μm, the A-SZO-S pathway can no longer sustain the full operating current, and the support gradually loses its effectiveness as an external current collection terminal. A finite S-A direct-current response nevertheless remains, indicating that the anode and support are not completely isolated. Although the effective S-A resistance exhibits an overall increasing tendency with SZO thickness, noticeable nonmonotonic variations are present. Nevertheless, the substantial decrease in S-C power output indicates that the current collection capability of the support is strongly suppressed for thicker SZO layers. Meanwhile, the gas permeability remains relatively high within this range, providing a favorable balance between electrical decoupling and gas transport. Accordingly, the highest A-C performance is obtained at an SZO thickness of approximately 73 μm.

When the SZO thickness reaches approximately 80 μm or greater, further electrical decoupling provides limited benefit. Meanwhile, the apparent gas permeability markedly decreases, indicating increased transport resistance through the thicker and more tortuous porous layer. Restricted H_2 supply and the removal of product H_2O may intensify local concentration gradients and mass transfer polarization on the anode side. Consequently, gas transport losses begin to outweigh the gains from electrical decoupling, leading to a renewed decrease in the A-C power density[31,32].

The favorable thickness window identified in this study is specific to the pore structures of the cermet support and SZO layer that were used. Increasing the connected porosity of either layer may reduce gas transport resistance and shift the onset of transport losses to greater SZO thicknesses. A higher SZO porosity may also reduce its effective solid-phase conductivity, allowing electrical decoupling at a smaller thickness. However, excessive or nonuniform porosity may introduce local defects, while variations in pore morphology, connectivity, and tortuosity can also influence the effective electrical transport and gas permeability of porous ceramic layers[33-35]. Conversely, lower porosity may increase gas transport resistance and narrow the favorable thickness window. Therefore, the optimum thickness should be considered a parameter that depends on the microstructure, including the layer thickness, porosity, pore connectivity, and tortuosity. In summary, the cell performance is governed by the competing effects of anode-support electrical coupling and gas transport resistance. Among the tested cells, the maximum A-C power density was obtained at an SZO thickness of approximately 73 μm. However, considering the combined requirements of effective electrical decoupling and sufficient gas permeability, a thickness range of approximately 73-80 μm was identified as the practical optimal window under the investigated conditions.

Electrochemical performance of the 12-cell FT-SIS-SOFC

Figure 9A summarizes the output performance and post-operation characterization of the 12-cell FT-SIS-SOFC. The device showed a total OCV of approximately 12 V at 700 °C, indicating that a series connection was successfully achieved and that electrical coupling between the anode and support was suppressed. As the temperature increased from 700 to 800 °C, the OCV slightly decreased, whereas the peak power density was approximately 68 mW cm^{-2} at 700 °C, 115 mW cm^{-2} at 750 °C, and 150 mW cm^{-2} at 800 °C.

Figure 9B shows that the impedance decreases significantly as the temperature increases from 700 to 800 °C. Figure 9C quantifies the ohmic resistance, polarization resistance, and total resistance at each temperature. The total resistance decreases from approximately 45 Ω cm^2 at 700 °C to approximately 18 Ω cm^2 at 800 °C. The polarization resistance decreases from approximately 28 Ω cm^2 at 700 °C to approximately 10 Ω cm^2 at 800 °C. Finally, the ohmic resistance decreases from approximately 17 to 8 Ω cm^2 as the temperature increases.

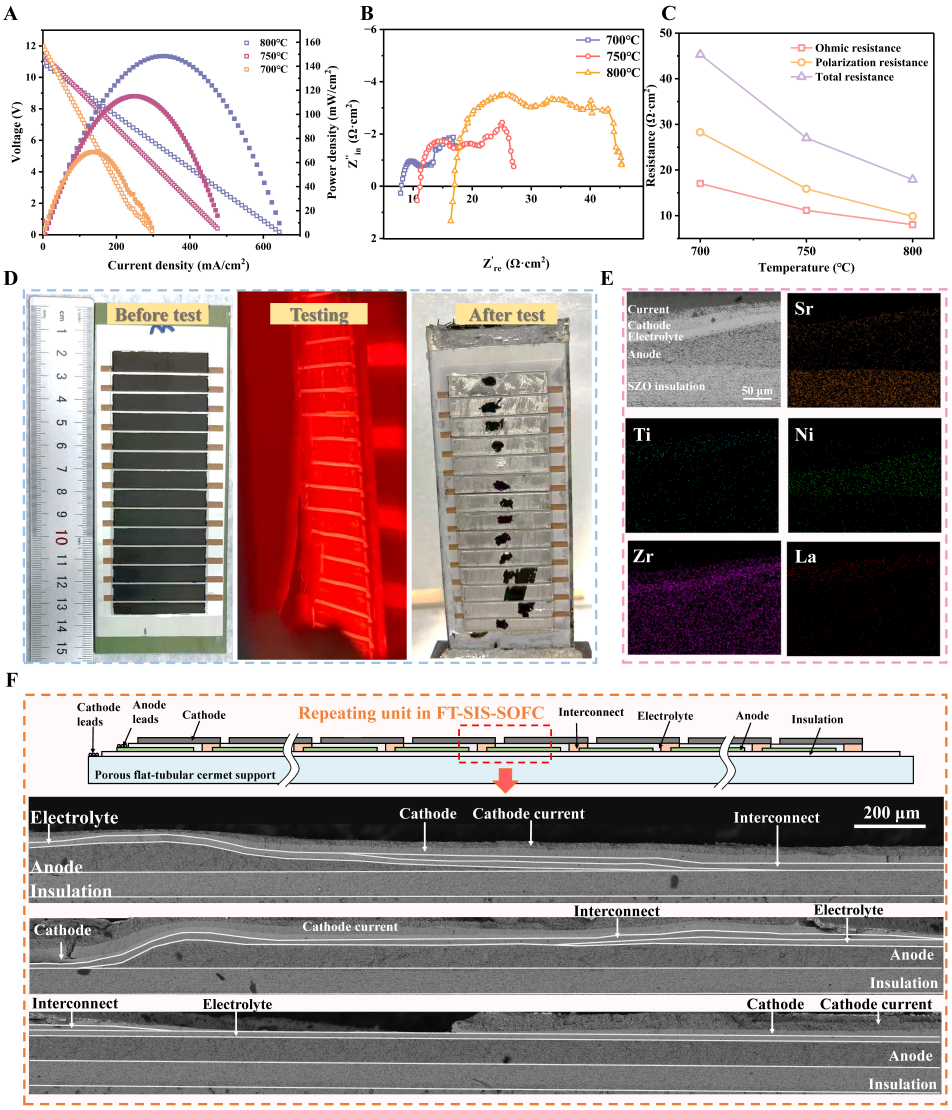


Figure 9. Output performance and post-operation characterization of the 12-cell FT-SIS-SOFC. (A) I-V-P curves; (B) impedance spectra; (C) fitted resistance components at different temperatures; (D) photographs of the FT-SIS-SOFC before testing, during high-temperature operation, and after testing, taken by the authors; (E) EDS elemental mapping after operation; and (F) cross-sectional SEM image of a repeating unit. The reported power densities were normalized to the total effective active area of the 12 cells (24 cm^2). FT-SIS-SOFC: Flat-tubular segment-in-series solid oxide fuel cell; SZO: $SrZrO_3$; EDS: energy-dispersive X-ray spectroscopy; SEM: scanning electron microscopy; I-V-P: current-voltage-power density curves.

The performance loss in this system occurred mainly under load and was associated with the cumulative internal resistance of the cells that were connected in series. The polarization resistance was consistently higher than the ohmic resistance, accounting for approximately 56%-62% of the total resistance. This indicates that the principal limitations were electrode kinetics, local gas transport, and nonuniformity between cells. The appreciable ohmic contribution was likely associated with the cumulative resistances of the electrolyte, interconnects, electrode current collection paths, and contacts between layers. In particular, interfacial contact resistance can contribute to the overall electrical losses in SOFC stacks[36]. The electrode-interconnect pathway had to carry the entire operating current, increasing the significance of the lateral current-collection and interfacial resistances.

Figure 9D compares the device appearance before testing, during operation, and after testing. No visible macroscopic cracking or structural collapse was observed after operation, and the overall layered structure

remained intact. Figure 9E shows the post-operation elemental mapping at the interfaces. The main elements are largely confined to their respective layers, with no obvious interdiffusion across layers detectable by EDS. Figure 9F further shows the cross-sectional morphology of a repeating unit after operation. The SZO insulating layer remains continuous, and the interfaces between adjacent layers remain distinguishable, although the cathode layer exhibits relatively low porosity and a longitudinal crack. This cathode microstructure may contribute to the limited overall power output, as previous studies have shown that cathode pore structure and interfacial defects can influence polarization and ohmic losses[37,38].

Overall, these results confirm that the porous SZO layer can function as an electrical isolator in a cermet-supported FT-SIS-SOFC and enable voltage addition in series. However, the device performance is still constrained by interfacial resistance and the cathode microstructure, suggesting that further optimization of the repeating unit geometry and cathode fabrication would be beneficial.

CONCLUSION

In this study, the effect of porous SZO insulating layer thickness on the electrical isolation and gas transport characteristics of cermet-supported FT-SIS-SOFCs was systematically investigated. Porous SZO was demonstrated as an effective insulating layer, where its thickness determines the balance between residual electrical coupling and gas transport resistance. Thin SZO layers resulted in incomplete electrical decoupling and additional polarization losses, whereas excessively thick layers increased gas transport limitations. The maximum A-C power density was achieved at an SZO thickness of approximately 73 μm, while the thickness range of 73-80 μm was identified as the practical optimal window, providing a favorable balance between electrical insulation and gas transport. Using this optimized design, a 14-cell FT-SIS-SOFC with 12 effective cells was successfully fabricated, achieving an open-circuit voltage of 12 V at 700 °C and a peak power density of 150 mW cm^{-2} at 800 °C. These findings provide a practical design strategy for porous insulating layers in high-voltage FT-SIS-SOFC architectures.

The present study is limited to the evaluation of SZO layers within the investigated thickness range and under the tested operating conditions. Further studies are required to clarify the long-term stability, thermal cycling durability, and degradation mechanisms of porous SZO insulating layers during extended operation. Future efforts will focus on optimizing the microstructure of the insulating layer and exploring scalable fabrication strategies for high-performance multi-cell FT-SIS-SOFC systems.

DECLARATIONS

Acknowledgments

The authors gratefully acknowledge the technical support provided by the Xi'an Advanced Functional Coating Technology International Science and Technology Cooperation Base.

Authors' contributions

Conceptualization, data curation, investigation, validation, visualization, writing - original draft: Chen, R.
Data curation, visualization: Pan, X.
Data curation: Jiao, H.
Investigation, validation: Ma, T.
Investigation: Li, Y.
Visualization: Xu, S.
Conceptualization, methodology, supervision, writing - review & editing: Liu, C.
Conceptualization, funding acquisition, project administration, resources, supervision, writing - review & editing: Li, C. X.

Availability of data and materials

All data supporting the findings of this study are available within the article and its Supplementary Materials files. Raw data are available from the corresponding author upon reasonable request.

AI and AI-assisted tools statement

Not applicable.

Financial support and sponsorship

This work was supported by the National Key Research and Development Program of China (No. 2021YFB4001400), Key Research and Development Plan of Shaanxi Province (No. S2023-YF-LLRH-QCYK-0201), and Research Project of Incubated Teams at Shaanxi Laboratory of Advanced Materials (No. 24GJSY0012-2025XCLSXSYS-RZ-01).

Conflicts of interest

Pan, X.; Jiao, H. are affiliated with Shandong Moon Hydrogen Technology Research Institute Co., Ltd., and Xu, S. is affiliated with Moon Environment Technology Co., Ltd. The authors declare no other conflicts of interest.

Ethical approval and consent to participate

Not applicable.

Consent for publication

Not applicable.

Copyright

© The Author(s) 2026.

Supplementary Materials

Supplementary Materials

REFERENCES

1. Sikstrom, D.; Thangadurai, V. A tutorial review on solid oxide fuel cells: fundamentals, materials, and applications. *Ionics* **2026**, *32*, 5-30. DOI PubMed PMC
2. Feng, P.; Yang, K.; Liu, X.; Zhang, J.; Li, Z. A review of advanced SOFCs and SOECs: materials, innovative synthesis, functional mechanisms, and system integration. *eScience* **2026**, *6*, 100460. DOI
3. Li, J.; Cheng, J.; Zhang, Y.; et al. Advancements in solid oxide fuel cell technology: bridging performance gaps for enhanced environmental sustainability. *Adv. Energy. Sustain. Res.* **2024**, *5*, 2400132. DOI
4. Torrigino, F.; Grimm, F.; Karl, J.; Herkendell, K. In-situ electrochemical impedance analysis of a commercial SOFC stack fueled by real wood gas. *Heliyon* **2024**, *10*, e32509. DOI PubMed PMC
5. Fan, J.; Shi, J.; Wang, Y.; Shi, Y. Numerical investigation of air flow characteristics for a compact 5 × 10 array tubular segmented-in-series solid oxide fuel cell stack. *Appl. Therm. Eng.* **2024**, *247*, 123039. DOI
6. Wu, Z.; Zhu, P.; Huang, Y.; et al. A comprehensive review of modeling of solid oxide fuel cells: from large systems to fine electrodes. *Chem. Rev.* **2025**, *125*, 2184-268. DOI PubMed PMC
7. Fan, J.; Shi, J.; Zhang, R.; Wang, Y.; Shi, Y. Numerical study of a 20-cell tubular segmented-in-series solid oxide fuel cell. *J. Power. Sources.* **2023**, *556*, 232449. DOI
8. Li, T.; Heenan, T. M. M.; Rabuni, M. F.; et al. Design of next-generation ceramic fuel cells and real-time characterization with synchrotron X-ray diffraction computed tomography. *Nat. Commun.* **2019**, *10*, 1497. DOI PubMed PMC
9. Lai, T. S.; Barnett, S. A. Design considerations for segmented-in-series fuel cells. *J. Power. Sources.* **2005**, *147*, 85-94. DOI
10. Cui, D.; Cheng, M. Design for segmented-in-series solid oxide fuel cell through mathematical modeling. *J. Power. Sources.* **2010**, *195*, 1435-40. DOI
11. Kobayashi, Y.; Tomida, K.; Nishiura, M.; Hiwatashi, K.; Kishizawa, H.; Takenobu, K. Development of next-generation large-scale SOFC toward realization of a hydrogen society. *Mitsubishi. Heavy. Ind. Tech. Rev.* **2015**, *52*, 111-6. https://www.mhi.com/technology/review/abstract-52-2-111 (accessed 2026-11-12).
12. Pandey, A.; Shyam, A.; Liu, Z.; Goettler, R. In-situ Young's moduli of the constitutive layers in a solid oxide fuel cell. *J. Power. Sources.* **2015**, *273*, 522-9. DOI
13. Chen, R.; Li, Y.; Li, J.; Liu, C.; Li, C. Flat-tubular segment-in-series solid oxide fuel cells: sinterability and conductivity synergistic enhancement of $La_{0.3}Sr_{0.7}TiO_3$ interconnects through Co_3O_4 modification. *ACS. Sustain. Chem. Eng.* **2025**, *13*, 21040-54. DOI

14. Ismail, S.; Khedr, G. E.; Salem, F. Z.; Allam, N. K. Defect-Engineered $SrZrO_3$: unraveling the role of nitrogen and carbon in optoelectronic and catalytic performance. *Energy. Fuels.* **2025**, *39*, 13703-14. DOI
15. Yamanaka, S.; Kurosaki, K.; Oyama, T.; et al. Thermophysical properties of perovskite-type strontium cerate and zirconate. *J. Am. Ceram. Soc.* **2005**, *88*, 1496-9. DOI
16. Singh, V.; Seshadri, M. Perovskite $SrZrO_3$:Ho^{3+} phosphors: synthesis, structure, Judd-Ofelt analysis and photoluminescence properties. *RSC. Adv.* **2023**, *13*, 27782-91. DOI PubMed PMC
17. Liu, Y.; Bai, Y.; Li, E.; et al. Preparation and characterization of $SrZrO_3$-$La_2Ce_2O_7$ composite ceramics as a thermal barrier coating material. *Mater. Chem. Phys.* **2020**, *247*, 122904. DOI
18. Chou, J.; Inoue, Y.; Kawabata, T.; Matsuda, J.; Taniguchi, S.; Sasaki, K. Mechanism of $SrZrO_3$ formation at GDC/YSZ interface of SOFC cathode. *J. Electrochem. Soc.* **2018**, *165*, F959-65. DOI
19. Kanae, S.; Toyofuku, Y.; Kawabata, T.; et al. Microstructural characterization of $SrZrO_3$ formation and the influence to SOFC performance. *ECS. Trans.* **2015**, *68*, 2463-70. DOI
20. Budiman, R.; Hapsari, A.; Damisih; et al. Mitigating $SrZrO_3$ phase formation at air electrode/electrolyte of solid oxide cell: a review. *J. Power. Sources.* **2025**, *655*, 238176. DOI
21. Labrincha, J.; Frade, J.; Marques, F. Defect structure of $SrZrO_3$. *Solid. State. Ionics.* **1993**, *61*, 71-5. DOI
22. Dunyushkina, L.; Khaliullina, A.; Meshcherskikh, A.; Pankratov, A.; Osinkin, D. Effect of a-site nonstoichiometry on defect chemistry and electrical conductivity of undoped and Y-doped $SrZrO_3$. *Materials* **2019**, *12*, 1258. DOI PubMed PMC
23. Hisai, Y.; Murakami, K.; Kamite, Y.; et al. First observation of surface protonics on $SrZrO_3$ perovskite under a H_2 atmosphere. *Chem. Commun.* **2020**, *56*, 2699-702. DOI
24. Huang, P.; Petric, A. Electrical conduction of yttrium-doped strontium zirconate. *J. Mater. Chem.* **1995**, *5*, 53. DOI
25. Müller, J.; Kreuer, K.; Maier, J.; Matsuo, S.; Ishigame, M. A conductivity and thermal gravimetric analysis of a Y-doped $SrZrO_3$ single crystal. *Solid. State. Ionics.* **1997**, *97*, 421-7. DOI
26. Yajima, T.; Suzuki, H.; Yogo, T.; Iwahara, H. Protonic conduction in $SrZrO_3$-based oxides. *Solid. State. Ionics.* **1992**, *51*, 101-7. DOI
27. Schober, T. Water vapor solubility and impedance of the high temperature proton conductor $SrZr_{0.9}Y_{0.1}O_{2.95}$. *Solid. State. Ionics.* **2001**, *145*, 319-24. DOI
28. An, Y.; Ji, M.; Hwang, H.; Eugene Park, S.; Choi, B. Effect of cell-to-cell distance in segmented-in-series solid oxide fuel cells. *Int. J. Hydrogen. Energy.* **2015**, *40*, 2320-5. DOI
29. Primdahl, S.; Mogensen, M. Gas conversion impedance: a test geometry effect in characterization of solid oxide fuel cell anodes. *J. Electrochem. Soc.* **1998**, *145*, 2431-8. DOI
30. Wang, Z. Distribution of relaxation times for impedance analysis in batteries and fuel cells. *Nat. Rev. Clean. Technol.* **2025**, *1*, 453-453. DOI
31. Yamazaki, K.; Kishimoto, M.; Iwai, H. Three-dimensional numerical simulation of counter gas transport in porous anodes of solid oxide fuel cells. *J. Power. Sources.* **2025**, *627*, 235766. DOI
32. Wei, Y.; Ning, Z.; Sun, C.; et al. Research on effect of anode microstructures on mass transfer and electrochemical reaction in SOFCs based on a fractional Brownian motion model. *J. Solid. State. Electrochem.* **2025**, *29*, 191-206. DOI
33. Chen, D.; Lin, Z.; Zhu, H.; Kee, R. J. Percolation theory to predict effective properties of solid oxide fuel-cell composite electrodes. *J. Power. Sources.* **2009**, *191*, 240-52. DOI
34. Celik, E.; Usler, A.; Wiche, M.; et al. Unexpectedly high electronic partial conductivity of porous yttria-stabilized zirconia thin films. *J. Phys. Chem. C.* **2025**, *129*, 12585-94. DOI
35. Langner, E.; Semenov, A.; Makradi, A.; Gouttebroze, S.; Belouettar, S.; Wallmersperger, T. Macroscopic properties of solid oxide fuel cell electrodes via microstructure-based numerical homogenization. *Proc. Appl. Math. Mech.* **2024**, *24*, e202400023. DOI
36. Shong, W.; Liu, C.; Kao, W.; Tsai, C.; Chang, C.; Cheng, Y. Effect of electric current on cathode-side contact resistance in SOFC stacks. *Int. J. Hydrogen. Energy.* **2025**, *100*, 863-9. DOI
37. Hou, L.; Zhang, M.; Zhang, S.; Hou, Y.; Lv, Y. Microstructural and electrochemical properties of $Gd_{0.3}Ba_{0.7}FeO_{3-\delta}$-$xCe_{0.90}Gd_{0.10}O_{1.95}$ composite cathode for solid oxide fuel cells. *Phys. Status. Solidi. A.* **2025**, *222*, 2400976. DOI
38. Shao, Y.; Shen, J.; Ren, H.; Zhao, L.; Xue, Z. The influence of microstructural evolution on performance degradation in solid oxide fuel cells. *Mater. Sci. Eng. B.* **2025**, *317*, 118187. DOI

Disclaimer/Publisher's Note: All statements, opinions, and data contained in this publication are solely those of the individual author(s) and contributor(s) and do not necessarily reflect those of OAE and/or the editor(s). OAE and/or the editor(s) disclaim any responsibility for harm to persons or property resulting from the use of any ideas, methods, instructions, or products mentioned in the content.



© The Author(s) 2026. Open Access This article is licensed under a Creative Commons Attribution 4.0 International License (https://creativecommons.org/licenses/by/4.0/), which permits unrestricted use, sharing, adaptation, distribution and reproduction in any medium or format, for any purpose, even commercially, as long as you give appropriate credit to the original author(s) and the source, provide a link to the Creative Commons license, and indicate if changes were made.